American Flame Research Committee
2024 Symposium
Calgary, Alberta
September 30 – October 3, 2024

Comparison of Long- and Mid-Wavelength Imaging Fourier Transform Spectrometers for Quantifying Flare Combustion Efficiency

A. R. Singh, P. Lapeyre, K. J. Daun
Department of Mechanical and Mechatronics Engineering, University of Waterloo
200 University Ave W, Waterloo ON, Canada

Abstract

This work aims to compare the capabilities of Imaging Fourier transform spectrometers (IFTSs) that operate in the long-wavelength infrared (LWIR) and mid-wavelength infrared (MWIR) range for quantifying flare combustion efficiency (CE). The two IFTSs were operated simultaneously to measure spectral intensities emitted by a steam-assisted flare at an oil refinery in Southern Ontario. Species column densities were inferred from the measured intensity spectra using a spectroscopic model, while the velocity field was obtained from feature tracking between successive images. Species mass flow rates were then derived by integrating the concentrations and normal velocity along a control line transecting the flare plume. The mass flow rate inferred from the LWIR-IFTS was 50 and 190 g/s for CO_2 and H_2O, respectively, in range with 70 and 150 g/s inferred from the MWIR-IFTS. Manual fingerprinting showed potential signs of C_2H_4, C_3H_6, and C_4H_{10} from the intensity spectra measured in the LWIR and MWIR. While this work demonstrates the potential for IFTS in remote sensing of flare CE, a more robust spectral fingerprinting algorithm is needed in order to obtain reliable CE estimates when the fuel is unknown.

1 Introduction

In the oil and gas industry, flaring is used to convert unwanted flammable gases, mainly hydrocarbons, into less harmful species like CO_2 [1]. Initially used for safety reasons, flaring is becoming increasingly important in the context of environmental stability due to the lower climate change potential of the combustion products compared to the hydrocarbons [2]. Flaring performance may be defined by combustion efficiency (CE), which is usually assumed to be close to 98% [3, 4]. However, external factors like cross wind or steam assistance may lower this value considerably [5, 6, 7, 8]. Consequently, flare operators and regulators urgently need remote sensing techniques to accurately quantify flare CE.

Imaging Fourier transform spectrometers (IFTS) are a promising instrument for flare CE quantification due to their high spectral resolution, and their ability to image the entire flare plume [9, 10, 11] as opposed to passive Fourier transform infrared spectroscopy (PFTIR), which can only resolve spectral emission along a single line-of-sight (LOS) [12]. These instruments generate a 3D data cube, consisting of two spatial dimensions and one spectral dimension at typical resolutions of 1 cm^{-1}. The CE is calculated by inferring species column densities and gas projected velocities for each pixel along a control line; the velocities and column densities are combined to obtain species mass flow rates [13, 14]. While the infrared range covered by the IFTS varies depending on the camera, both long-wavelength infrared (LWIR) and mid-wavelength infrared (MWIR) spectral ranges contain rotational and vibrational bands for the key species important to flare CE [15, 16]. However, a qualitative comparison between these camera types highlights that the LWIR IFTS may be more accurate because of its ability to detect hot gases as well as cold gases (e.g. cold pockets of fuel stripped outside of the combustion zone in the presence of cross-wind) [16]. In this work, a simultaneous measurement of a petrochemical flare with both LWIR- and MWIR-IFTS is conducted for the purpose of computing the flare CE.

2 Flare Combustion Efficiency

Flare CE can be defined as the ratio of mass flow rates of carbon affixed to CO_2 ($\dot{m}_{C,CO2}$) to the carbon entering the flare stack via the fuel ($\dot{m}_{C,fuel}$). In standoff estimates where the fuel type may be unknown, the mass flow rate of carbon affixed to the fuel can be approximated as the sum of mass flow rates of carbon contained in all species leaving the flare plume. This definition may be expressed as

$$\mathrm{CE} = \frac{\dot{m}_{\mathrm{C,\,CO_2}}}{\dot{m}_{\mathrm{C,\,fuel}}} \approx \frac{\dot{m}_{\mathrm{C,\,CO_2}}}{\sum_k \dot{m}_{\mathrm{C},\,k}} \tag{1}$$

The mass flow rate of carbon affixed to the k^{th} species is found by integrating the product of the species column density and velocity along a control line (Θ) that transects the flare plume in the infrared image, and then multiplying by the mass fraction of carbon within the k^{th} species:

$$\dot{m}_{C,k} = \frac{M_C}{M_k}\dot{m}_k = \frac{M_C}{M_k}\int_\Theta \rho_k(\theta) V_n(\theta)\, d\theta \tag{2}$$

where M_C is the combined molar mass of carbon within the k^{th} species (e.g., M_C = 12 g/mol for CO_2 while M_C = 24 g/mol for C_2H_4), M_k is the molecular molar mass of the k^{th} species, ρ is the column density (kg/m^2), V_n is the velocity component (m/s) normal to the control line Θ, and θ refers to a local position on Θ.

In Eq. (2), the column density of the k^{th} species can be calculated from the ideal gas law, and is derived as

$$\rho_k(\theta) = \frac{M_k p}{k_B N_A}\int_{LOS(\theta)} \frac{\chi_k(s,\theta)}{T(s,\theta)} ds \tag{3}$$

where p is ambient pressure (kPa), k_B is Boltzmann's constant, N_A is Avogadro's number, $\chi_k(s, \theta)$ is mole fraction of the k^{th} species at location s on a pixel LOS that pierces θ, and T is the plume temperature (K). Note that $\chi_k \times 10^6$ represents concentration of the k^{th} species in parts-per-million (ppm). The normal velocity V_n in Eq. (2) can be calculated by tracking the motion of turbulent structures within the plume between successive images. The unknowns for evaluating flare CE are the distributions of mole fraction $\chi_k(s, \theta)$ and plume temperature $T(s, \theta)$ along a control line, and normal velocity V_n, which are all inferred from spectral intensities of infrared light measured by an IFTS.

3 Experimental Methodology

3.1 IFTS operating principle

An IFTS detects the incoming infrared light using a Michelson interferometer. As seen in Figure 1, the incoming light is split into two paths by a beam splitter. The two beams are reflected by a mirror, recombined at the beam splitter, and then imaged onto a focal plane array (FPA). In one path, the mirror position and distance travelled by the light is fixed, while in the other the mirror moves during the measurement interval. The differences between these pathlengths induces constructive and destructive interference patterns in the intensity. Images captured at each distinct mirror position results in an interferogram data cube, which is then Fourier transformed and then calibrated to produce an absolute intensity data cube [17].

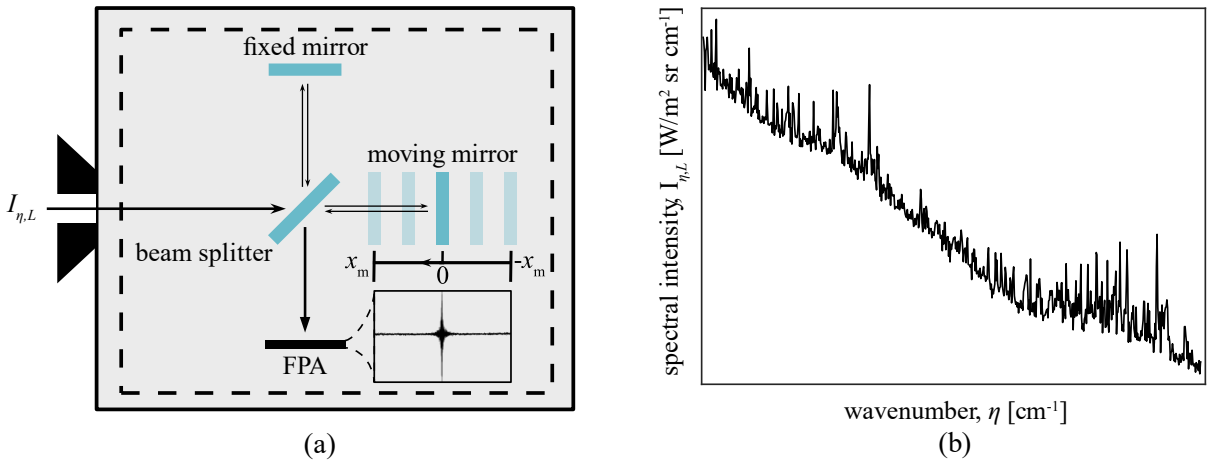

(a) (b)

Figure 1: Schematic of Michelson interferometer (a) inside an IFTS with inset showing a raw interferogram from one pixel detected by the FPA, which is processed by Fourier transformation and calibrated into an (b) intensity spectrum.

3.2 Measuring infrared light using an IFTS

In this study, two IFTSs over the LWIR (Telops Hyper-Cam Mini xLW, 750-1345 cm^{-1}) and MWIR (Telops Hyper-Cam MW, 2000-3300 cm^{-1}) were used to simultaneously image a steam-assisted flare at a petrochemical refinery in Southern Ontario. The two cameras were each mounted on their own tripods positioned within approximately 2 meters of each other and aimed towards a flare stack located 582 m away. The camera parameters were set according to Table 1 then individually calibrated using two built-in blackbody plates, each set at a unique temperature for two-point calibration. After calibration, the cameras were simultaneously set to measure the flare stack for approximately 30 minutes, over which time the LWIR- and MWIR-IFTS collected 210 and 43 data cubes, respectively.

The rapid motion of turbulent features in the flare plume causes fluctuations in the interferogram due to the finite time required to form the interferogram, leading to scene change artefacts in the transformed intensity spectrum. In this work, these artifacts were removed by calculating the median intensity for each pixel over all the data cubes [18].

Table 1: Parameters set for the LWIR- and MWIR-IFTS.

Parameters	Units	LWIR-IFTS	MWIR-IFTS
Image size	Pixel count	184 × 120	128 × 128
Image size	m	81.4 × 53.1	26.1 × 26.1
Frame rate	Hz	1046	748
Integration time	μs	116	100
Spectral resolution	cm^{-1}	1	1

3.3 Inferring species concentration and plume temperature

Concentration and temperature of species within the flare plume can be inferred from spectral intensities measured by an IFTS. The relationship between the physical properties of a gas and its infrared signature arises from molecular vibrations that cause its dipole moment to fluctuate (e.g., asymmetric stretching of atomic bonds in CO_2). These fluctuations interact with the surrounding electromagnetic field, leading to absorption of infrared light at the same frequency as the molecular vibration. The magnitude of infrared light that is absorbed scales with concentration and temperature of a gas, and the quantitative relationship is defined by the radiative transfer equation (RTE).

Species concentration and plume temperature at each pixel were found by regressing a modeled spectral intensity incident on the camera aperture along a pixel LOS, shown schematically in Figure 2, to the measured intensity. The model also assumes a static scene, as well as a uniform concentration and temperature profile along each pixel LOS. Under these conditions, the non-scattering RTE reduces to

$$I_{\eta,L} = \underbrace{\exp\left(-\kappa_{\eta,\,\mathrm{amb}} L_{\mathrm{amb}}\right)}_{\substack{\text{attenuation by}\\ \text{ambient gas layer}}} I_{\eta,\,\mathrm{interface}} + \underbrace{\left[1-\exp\left(-\kappa_{\eta,\,\mathrm{amb}} L_{\mathrm{amb}}\right)\right]}_{\substack{\text{spectral emittance of}\\ \text{ambient gas layer}}} I_{\eta,\,\mathrm{amb}} \tag{4}$$

where $I_{\eta,L}$ is the intensity entering the camera aperture, $I_{\eta,\,\mathrm{amb}}$ is the spectral intensity of a blackbody at ambient temperature, and $I_{\eta,\,\mathrm{interface}}$ is the spectral intensity leaving the interface between the flare plume and ambient gas layer given by

$$I_{\eta,\,\mathrm{interface}} = \underbrace{\exp\left(-\kappa_{\eta,\,\mathrm{plume}} L_{\mathrm{plume}}\right)}_{\substack{\text{attenuation by}\\ \text{flare plume layer}}} I_{\eta,\,\mathrm{bg}} + \underbrace{\left[1-\exp\left(-\kappa_{\eta,\,\mathrm{plume}} L_{\mathrm{plume}}\right)\right]}_{\substack{\text{spectral emittance of}\\ \text{flare plume layer}}} I_{\eta,\,\mathrm{plume}} \tag{5}$$

where $I_{\eta,\,\mathrm{plume}}$ is the spectral intensity of a blackbody at the flare plume temperature. The ambient temperature was measured by an onboard thermocouple to calculate $I_{\eta,\,\mathrm{amb}}$, while $I_{\eta,\,\mathrm{bg}}$ was approximated from the average spectral intensity measured at select pixels just outside the plume region. With the assumption that the flare plume is axisymmetric, the plume length, L_{plume}, was inferred from the infrared image captured by the IFTS.

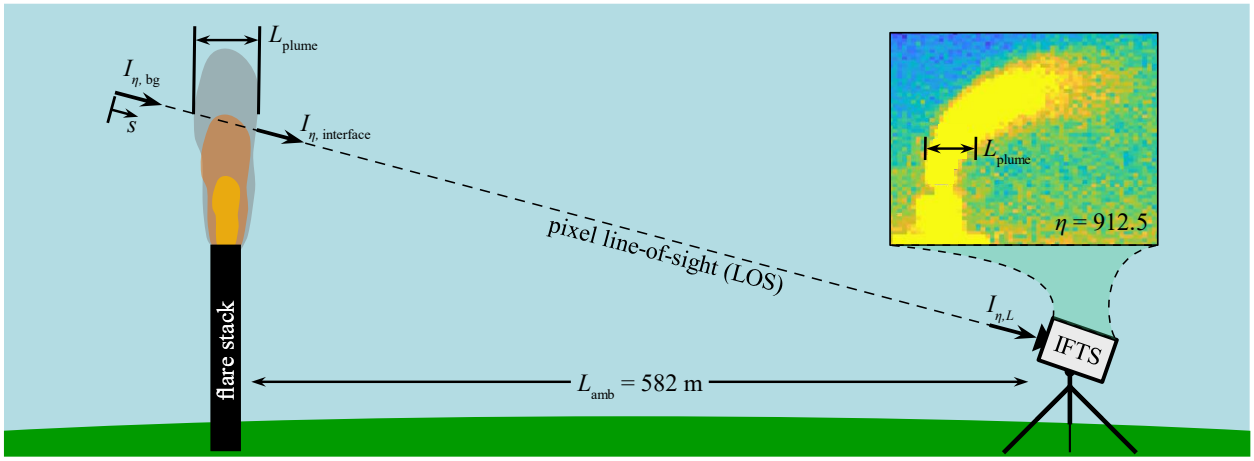

Figure 2: Schematic diagram of an IFTS pointed at a flare plume, with nomenclature for Eqs. (4) and (5).

In Eqs. (4) and (5), κ_η is the spectral absorption coefficient of the indicated layer, and is computed by summing the spectral absorption coefficients of each species in the layer

$$\kappa_\eta = \sum_k \kappa_{\eta,k}\left(\chi_k, T\right) \tag{6}$$

The spectral absorption coefficient for the k^{th} species depends on the mole fraction χ_k and plume temperature T (assuming that all species are at atmospheric pressure) and can be found on spectral line databases like HITRAN. In

practice, the values of χ_k and T in Eq. (6) are repeatedly adjusted until the modelled intensity $I_{\eta,L}$ from Eq. (4) matches the measured intensity spectrum for a given pixel.

3.4 Inferring the velocity field

The two-dimensional velocity field, $V = [V_x, V_y]^T$, was inferred from raw interferometer images that were normalized and filtered (i.e., mean intensity of frame subtracted) to remove stationary features prior to applying an optical flow algorithm. The change in the brightness pattern between two successive frames is modelled by taking the derivative of a pixel brightness B with respect to time t, and assuming that changes in the pixel brightness are only the result of objects traversing space, leading to

$$\frac{\partial B}{\partial x}V_x + \frac{\partial B}{\partial y}V_y + \frac{\partial B}{\partial t} = 0 \tag{7}$$

Here, the spatial and temporal gradients are pre-computed from the images via finite difference approximations. The underdetermined system of one equation and two unknowns (V_x and V_y) was solved using the Lucas-Kanade method [19], which assumes the velocity field within a window of n pixels is uniform. The number of pixels within the window is typically $n > 2$, leading to an overdetermined system of n equations and two unknowns. For a given window of n pixels, least squares minimization with a weighting scheme biasing the center pixel is used to determine the optimal combination of V_x and V_y that best satisfy all n equations simultaneously. The calculated velocity field can then be used to estimate the mass flow rate of flare plume species and flare CE.

4 Results and Discussion

4.1 Quantification of plume species with guaranteed presence

The veracity of the present work was confirmed by comparing mass flow rates inferred from spectral intensities measured by the LWIR- and MWIR-IFTSs of CO_2 and H_2O, which are the dominant species in the flare plume. For each pixel, the mole fractions of the two species (required for mass flow rate calculation) were inferred by fitting modelled intensities to the spectra measured between 750-820 cm^{-1} from the LWIR-IFTS and 2000-2400 cm^{-1} from the MWIR-IFTS. Figure 3 shows an example spectral fit for a single flare plume pixel. The selected spectral ranges were expected to contain absorption features exclusive to CO_2 and H_2O, with the caveat that potential trace of CO also has absorption features between 2000-2400 cm^{-1}. Consequently, the mole fraction of CO was also inferred from the MWIR data to avoid overestimating mole fractions of CO_2 and H_2O in the 2000-2400 cm^{-1} range.

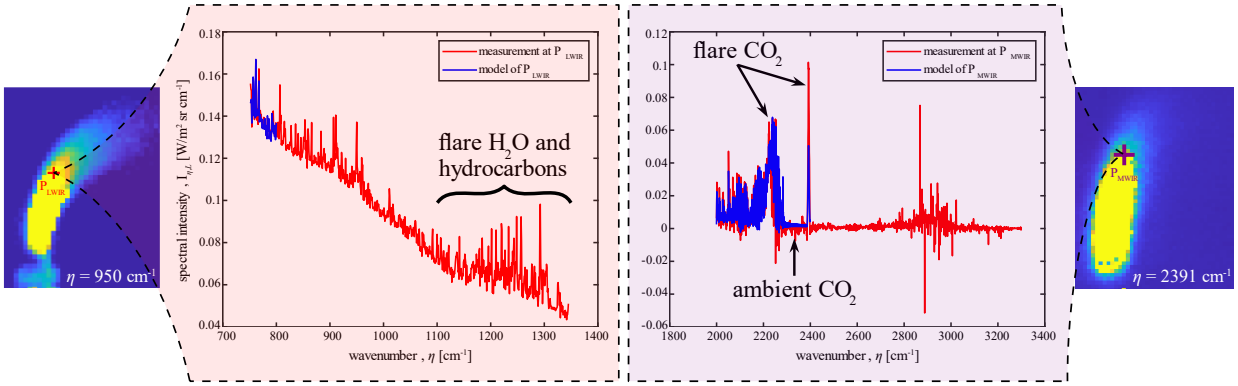

(a) (b)

Figure 3: Modelled and measured spectral intensities from (a) LWIR- and (b) MWIR-IFTS for quantification of CO_2 and H_2O at pixel P_{LWIR} and P_{MWIR} shown in the infrared image at 950 and 2391 cm^{-1}, respectively.

The measured LWIR spectrum in Figure 3a shows prominent features of H_2O in the 1100-1345 cm^{-1} range that were excluded in the model fit because the region is contaminated by absorption features of potential hydrocarbons such as methane (CH_4). In the MWIR spectrum shown in Figure 3b, the modelled and measured spectra show emission features at 2250 and 2400 cm^{-1} caused by the hot CO_2 in the flare plume. The flat section between the two peaks is a result of absorption from CO_2 at ambient temperature in the ambient layer between the flare plume and IFTS.

The inferred mole fraction and plume temperature distributions of CO_2 and H_2O along a control line transecting the flare plume are shown in Figure 4c from the LWIR-IFTS, and Figure 4d from the MWIR-IFTS. Considering only the flare plume region, the mole fraction peaks of CO_2 and H_2O inferred from the LWIR-IFTS are 1.5×10^{-3} and 1.7×10^{-2}, respectively, consistent with the inferred peaks of 4.6×10^{-3} and 1.6×10^{-2} from the MWIR-IFTS. While the LWIR-IFTS does not detect absorption features pertaining to CO, trace quantities of CO were inferred from the

MWIR-IFTS. Figure 4e and Figure 4f show the species column densities resulting from Eq. (3) and velocity profile normal to the control line. The gap between ρ_{CO2} and ρ_{H2O} is smaller in comparison to the gap between χ_{CO2} and χ_{H2O} because CO_2 is heavier than H_2O. Meanwhile, peak normal velocities agree within 1% between the two IFTSs.

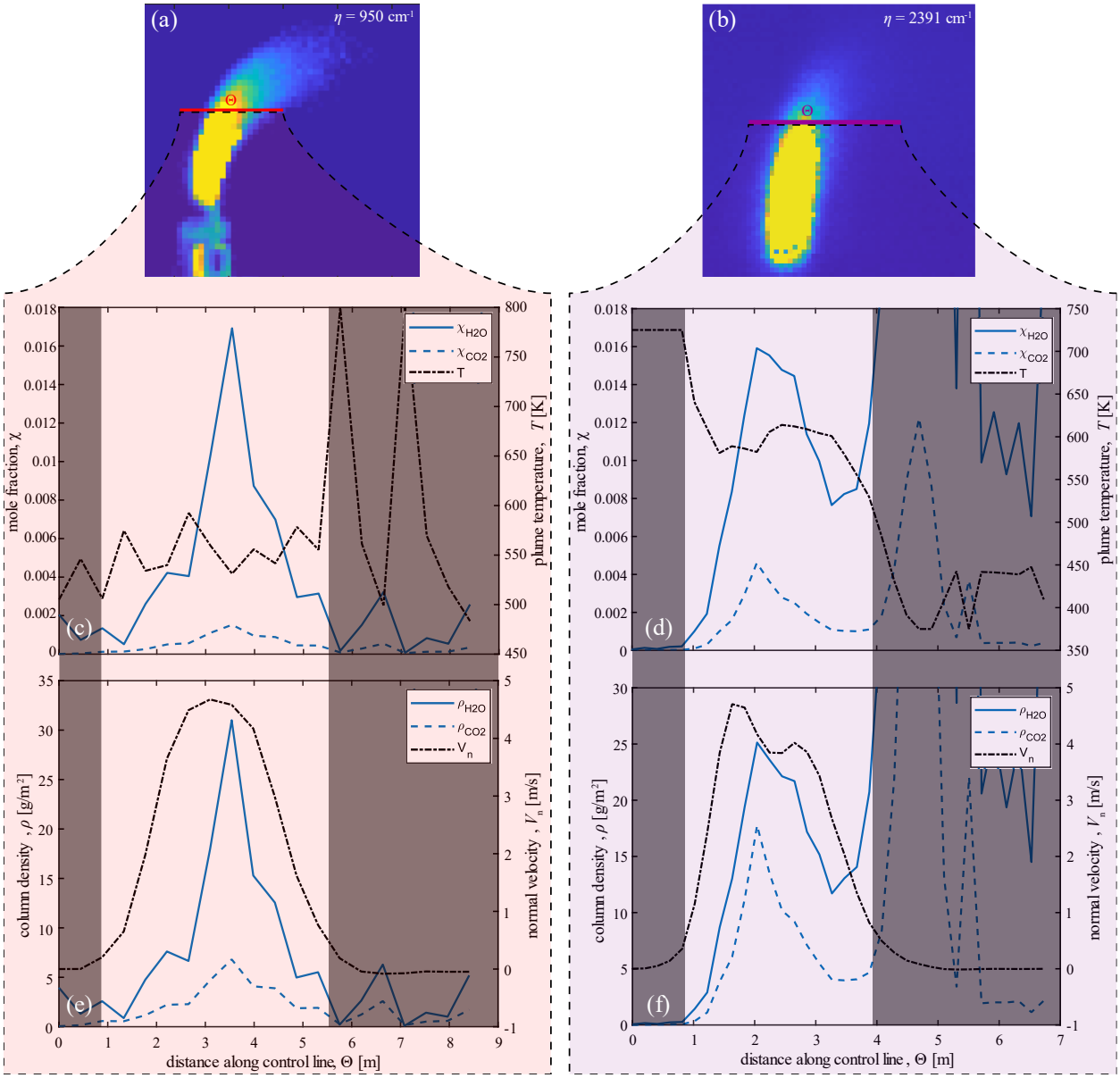

Figure 4: (a, b) Intensity contour, (c, d) distributions of χ_k and T, and (e, f) distributions of ρ_k and V_n along control line Θ from the LWIR- (a, c, e) and MWIR-IFTS (b, d, f). Regions outside the flare plume are shaded out.

The resulting mass flow rates inferred from the LWIR- and MWIR-IFTS are summarized in Table 2. The mass flow rate of H_2O ($\dot{m}_{H2O}$) being more than twice as high as the mass flow rate of CO_2 ($\dot{m}_{CO2}$) corroborates with the fact that the flare was steam-assisted during data collection. The mass flow rate differences between the two IFTSs are 29% and 27% for $\dot{m}_{CO2}$ and $\dot{m}_{H2O}$, respectively. While the inferences between the IFTS are within the same order of magnitude, agreement is expected to improve by reducing noise in the measured MWIR spectra (Figure 3b).

Table 2: Mass flow rates of CO_2 and H_2O in the flare plume, and the difference between the two IFTSs.

Species mass flow rate	**LWIR-IFTS**	**MWIR-IFTS**	**Difference**
Carbon dioxide, $\dot{m}_{CO2}$	50 g/s	70 g/s	29%
Water vapour, $\dot{m}_{H2O}$	190 g/s	150 g/s	27%

4.2 Species fingerprinting for estimating flare CE

Hydrocarbons present within the flare plume must be identified and quantified to calculate the flare CE. The intensity spectrum modelled for CO_2 and H_2O are compared with the spectrum measured by the LWIR-IFTS in Figure 5a. Discrepancies between the model and measurement can be observed in the 900-1000 cm^{-1} range along with a distinct peak measured at 950 cm^{-1} that is not captured by the model. An infrared correlation table [20] shows that the alkene functional group has strong absorption features in the 900-1000 cm^{-1} range. Spectral signatures of the two simplest alkene molecules, ethylene (C_2H_4) and propene (C_3H_6), appear to answer the discrepancies in Figure 5a. Meanwhile, from the intensity spectrum measured by the MWIR-IFTS in Figure 5b, a distinct series of features in the 2800-3000 cm^{-1} range is left unexplained by the intensity model for CO_2, H_2O and CO. This clue paired with emissions data from National Pollutant Release Inventory (NPRI, [21]) suggest that butane (C_4H_{10}) may be present in the flare plume.

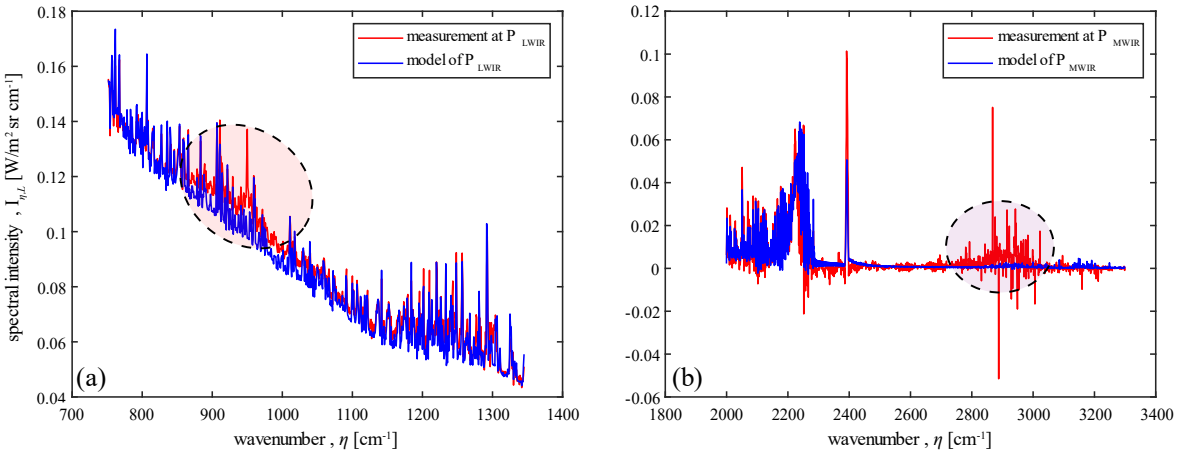

Figure 5: Modelled and measured intensity spectra for pixels (a) P_{LWIR} and (b) P_{MWIR} shown in Figure 3. Model accounts for CO_2 and H_2O (and CO for MWIR-IFTS). Shaded regions highlight discrepancies between model and measurement.

In Figure 6, updated model predictions accounting for C_2H_4, C_3H_6, and C_4H_{10} show improved fits against the measured spectra. However, detailed views of both LWIR and MWIR spectra show persistent disagreement between the model and measurement, suggesting that the selected combination of hydrocarbons is inconsistent with the actual hydrocarbons present within the flare plume. By incorrectly assuming the flare plume hydrocarbons are C_2H_4, C_3H_6, and C_4H_{10}, the inferred total mass flow rate of carbon affixed to the fuel needed in the denominator of Eq. (1) would have unquantifiable errors, and so too would the resulting flare CE. The lack of agreement between model and measurement in Figure 6 highlights the limitations of manually fingerprinting species, and the need for more advanced algorithms for accurate species detection for reliable estimations of flare CE. Until this automated algorithm is developed, prior information regarding the flare fuel would have to be known.

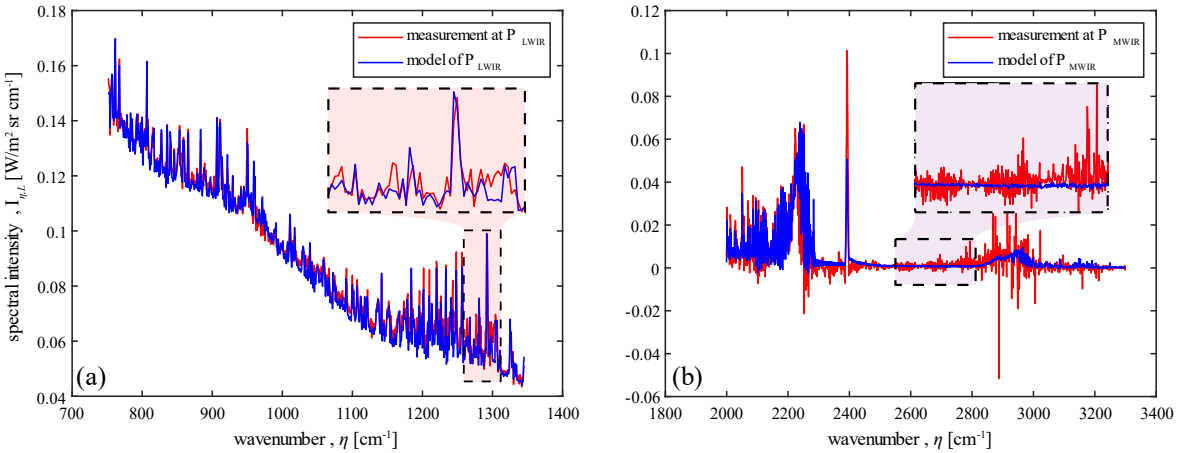

Figure 6: Modelled spectral intensity accounting for CO_2, H_2O, C_2H_4, C_3H_6, and C_4H_{10} (and CO for MWIR in (b)) fitted against spectral intensity measured at pixels (a) P_{LWIR} and (b) P_{MWIR} shown in Figure 3.

Future work in the short term will focus on collecting additional data cubes from the MWIR-IFTS to reduce the signal-to-noise ratio in the median-filtered spectral intensities, particularly in the 2500-3300 cm^{-1} range seen in Figure 6b where most hydrocarbons exhibit spectral signatures. Improving the signal-to-noise ratio of the MWIR spectra will considerably improve the reliability of manual and automated species fingerprinting. Improvements will also be made to the spectroscopic model by accounting for non-uniformity of species concentrations and temperature within the flare plume [14]. Future work in the long term includes developing a physics-based Bayesian model accelerated with machine learning to predict and quantify unknown species along with their uncertainty and building a full-scale flare stack for model validation. These tasks will help improve the accuracy and reliability of estimating flare CE from standoff measurements using an IFTS.

5 Conclusions

The high spatial and spectral resolution of IFTS makes it a promising instrument for monitoring green house gases from a standoff distance. This work focused on comparing a LWIR- and MWIR-IFTS for the purpose of estimating flare CE. The two IFTS were setup to simultaneously measure spectral intensities from a steam-assisted petrochemical flare stack. A spectroscopic model was fitted to the measured spectral intensities to quantify the concentrations of species present in the flare plume. This was combined with a feature tracking algorithm to infer the velocity field. The mass flow rates of species in the flare plume were obtained from the concentrations and velocity field estimates. The mass flow rates of CO_2 and H_2O were inferred as 50 and 190 g/s from the LWIR-IFTS, similar to 70 and 150 g/s inferred from the MWIR-IFTS. The higher release rate of H_2O relative to CO_2 is expected for steam-assisted flares. While manual fingerprinting of hydrocarbons suggested the presence of C_2H_4, C_3H_6, and C_4H_{10} in the flare plume, further comparisons of model and measured spectra suggested the true combination of hydrocarbons to differ. Accurate identification of the hydrocarbons present in the flare plume is required for reliable estimates of flare CE. This work demonstrates the potential for IFTS in the application of remote sensing and environmental monitoring, with further work needed in the area of automated species fingerprinting.

Acknowledgments

This research was sponsored by NSERC's FlareNet (NETGP 479641-15). The authors are grateful to Caroline Turcotte and Defence Research and Development Canada (DRDC) for loaning their MWIR-IFTS.

References

[1] A. Ahsan, H. Ahsan, J. S. Olfert and L. W. Kostiuk, "Quantifying the carbon conversion efficiency and emission indices of a lab-scale natural gas flare with internal coflows of air or steam," *Experimental Thermal and Fluid Science,* vol. 103, p. 133–142, 2019.

[2] C. N. Hewitt, "The atmospheric chemistry of sulphur and nitrogen in power station plumes," *Atmospheric Environment,* vol. 35, p. 1155–1170, 2001.

[3] U. S. E. O. of Air Quality Planning and S. (OAQPS), *Parameters for Properly Designed and Operated Flares,* 2012.

[4] D. M. Leahey, K. Preston and M. Strosher, "Theoretical and observational assessments of flare efficiencies," *Journal of the Air & Waste Management Association,* vol. 51, p. 1610–1616, 2001.

[5] M. R. Johnson, D. J. Wilson and L. W. Kostiuk, "A fuel stripping mechanism for wake-stabilized jet diffusion flames in crossflow," *Combustion Science and Technology,* vol. 169, p. 155–174, 2001.

[6] M. Zamani, E. Abbasi-Atibeh, S. Mobaseri, H. Ahsan, A. Ahsan, J. S. Olfert and L. W. Kostiuk, "An experimental study on the carbon conversion efficiency and emission indices of air and steam co-flow diffusion jet flames," *Fuel,* vol. 287, p. 119534, 2021.

[7] WorldBank, *Global Gas Flaring Tracker Report,* 2023.

[8] G. Plant, E. A. Kort, A. R. Brandt, Y. Chen, G. Fordice, A. M. Gorchov Negron, S. Schwietzke, M. Smith and D. Zavala-Araiza, "Inefficient and unlit natural gas flares both emit large quantities of methane," *Science,* vol. 377, p. 1566–1571, 2022.

[9] K. C. Gross, K. C. Bradley and G. P. Perram, "Remote identification and quantification of industrial smokestack effluents via imaging Fourier-transform spectroscopy," *Environmental science & technology,* vol. 44, p. 9390–9397, 2010.

[10] J. L. Harley and K. C. Gross, "Remote quantification of smokestack effluent mass flow rates using imaging Fourier transform spectrometry," in *Chemical, Biological, Radiological, Nuclear, and Explosives (CBRNE) Sensing XII*, 2011.

[11] S. Savary, J.-P. Gagnon, K. Gross, P. Tremblay, M. Chamberland and V. Farley, "Standoff identification and quantification of flare emissions using infrared hyperspectral imaging," in *Advanced Environmental, Chemical, and Biological Sensing Technologies VIII*, 2011.

[12] J. Wormhoudt, S. C. Herndon, J. Franklin, E. C. Wood, B. Knighton, S. Evans, C. Laush, M. Sloss and R. Spellicy, "Comparison of remote sensing and extractive sampling measurements of flare combustion efficiency," *Industrial & engineering chemistry research,* vol. 51, p. 12621–12629, 2012.

[13] R. B. Miguel, S. Talebi-Moghaddam, M. Zamani, C. Turcotte and K. J. Daun, "Assessing flare combustion efficiency using imaging Fourier transform spectroscopy," *Journal of Quantitative Spectroscopy and Radiative Transfer*, vol. 273, p. 107835, 2021.

[14] S. J. Grauer, B. M. Conrad, R. B. Miguel and K. J. Daun, "Gaussian model for emission rate measurement of heated plumes using hyperspectral data," *Journal of Quantitative Spectroscopy and Radiative Transfer,* vol. 206, p. 125–134, 2018.

[15] P. Lapeyre, R. B. Miguel, M. C. Nagorski, J.-P. Gagnon, M. Chamberland, C. Turcotte and K. J. Daun, "Quantifying flare combustion efficiency using an imaging Fourier transform spectrometer," *Journal of the Air & Waste Management Association,* vol. 74, p. 319–334, 2024.

[16] P. Lapeyre, N. S. Narayanan, M. Larivière-Bastien and K. J. Daun, "Quantifying flare combustion efficiency using a long wave infrared Fourier transform spectrometer," *Proceedings of the Combustion Institute,* vol. 40, p. 105554, 2024.

[17] H. E. Revercomb, H. Buijs, H. B. Howell, D. D. LaPorte, W. L. Smith and L. A. Sromovsky, "Radiometric calibration of IR Fourier transform spectrometers: solution to a problem with the High-Resolution Interferometer Sounder," *Applied Optics,* vol. 27, p. 3210–3218, 1988.

[18] J. L. Harley, B. A. Rankin, D. L. Blunck, J. P. Gore and K. C. Gross, "Imaging Fourier-transform spectrometer measurements of a turbulent nonpremixed jet flame," *Optics letters,* vol. 39, p. 2350–2353, 2014.

[19] B. D. Lucas and T. Kanade, "An iterative image registration technique with an application to stereo vision," in *IJCAI'81: 7th international joint conference on Artificial intelligence*, 1981.

[20] D. W. Ball, Physical Chemistry, Thomson Brooks/Cole, 2011.

[21] ECCC, *National Pollutant Release Inventory Map,* 2023.